

Swift heavy ion irradiation of InP: Thermal spike modeling of track formation

A. Kamarou,¹ W. Wesch,¹ E. Wendler,¹ A. Undisz,² and M. Rettenmayr²

¹*Institut für Festkörperphysik, Friedrich-Schiller-Universität Jena, Max-Wien-Platz 1, D-07743 Jena, Germany*

²*Institut für Materialwissenschaft und Werkstofftechnologie, Friedrich-Schiller-Universität Jena, Löbdergraben 32, D-07743 Jena, Germany*

(Received 6 December 2005; revised manuscript received 24 March 2006; published 5 May 2006)

Irradiation of single-crystalline InP with swift heavy ions (SHI's) causes the formation of ion tracks for certain irradiation temperatures if the electronic energy deposition exceeds a threshold value. With increasing SHI fluence, more and more ion tracks are formed, until a continuous amorphous layer is produced due to the multiple overlapping of the tracks at high ion fluences. Single-crystalline InP samples were irradiated either at liquid nitrogen temperature (LNT) or at room temperature (RT) with Kr, Xe, or Au ions with specific energies ranging from ca. 0.3 to 3.0 MeV/u. Afterwards, the samples were investigated by means of Rutherford back-scattering spectrometry and transmission electron microscopy in the plan-view and cross-section geometry. We show that the experimental data obtained can be qualitatively and quantitatively described on the basis of the inelastic thermal spike (TS) model, which was originally used only for metallic targets. The presented extension of the TS model on semiconductors covers mainly the very first stage of the energy transfer from SHI's (so-called "ionization spikes"). Our results show that the **extended TS model offers a self-consistent way to explain the influence of various irradiation conditions (ion mass, ion energy, irradiation temperature, etc.) on the ion track formation and damage accumulation in InP** and, therefore, can make a contribution to a better understanding of the underlying mechanisms. Further, our results prejudice the amenity of a *single value* of the threshold electronic energy loss as a fundamental quantity that is commonly used for the description of track formation in solids irradiated with *different ion species*. There is no universal RT threshold for track formation in InP, but it is noticeably higher for lighter ions (12.0 and 14.8 keV/nm for RT irradiations with Au and Xe, respectively). Our experimental and simulation results support the idea that the formation of visible tracks requires a predamaging of the material, unless each SHI penetrating *perfectly ordered virgin* InP directly produces a track that is large enough to be stable.

DOI: [10.1103/PhysRevB.73.184107](https://doi.org/10.1103/PhysRevB.73.184107)

PACS number(s): 61.80.Jh, 61.82.Fk, 81.05.Ea

I. INTRODUCTION

Ion implantation into semiconductors is a well-established technique used to modify electrical, optical, mechanical, and other physical properties of materials in defined regions. A demand to form thick buried layers (gettering layers, active layer-substrate isolation, power electronics applications, etc.) leads to the necessity for higher ion beam energies (MeV range instead of conventional tens or hundreds of keV). This is obviously connected with a drastic increase in the electronic energy deposition.¹ Contrary to the case of conventional ion energies, for MeV energies the electronic energy deposition per ion and unit path length ϵ_e is in the same order or dominates the nuclear one, ϵ_n .

Indium phosphide (InP) is known to have outstanding properties well suited for various electronic and optoelectronic applications.² Complex effects of radiation damage formation, transformation, and annealing due to high ϵ_e have been observed in recent decades in InP.^{3–11} Therefore, in order to be able to predict the damage distribution resulting from MeV ion implantation under various irradiation conditions, the influence of electronic energy deposition must be studied carefully. One possible way to do this is to use ion beams with energies in the range of several hundreds of MeV, for which ϵ_e near the surface is two or more orders of magnitude higher than ϵ_n and, thus, the maxima of the ϵ_e and ϵ_n depth distributions are well separated from each other.

Previously, Herre *et al.*,³ Wesch *et al.*,⁴ Gaiduk *et al.*,⁵ Szenes *et al.*,⁶ and Khalil *et al.*¹⁰ reported on the formation of continuous and discontinuous amorphous tracks, and a high pressure (wurtzite) phase within a depth region of dominating electronic energy deposition for single-crystalline InP irradiated with various swift heavy ions (SHI's). Higher SHI fluences cause track overlapping and formation of extended amorphous layers at sufficiently high ion fluence. It was also shown that there exists a threshold (minimum) value of the electronic energy loss ϵ_e^{thr} necessary to produce amorphous ion tracks (ca. 13 keV/nm as reported for 250 MeV Xe irradiation at room temperature³). This makes it possible to distinguish qualitatively between subthreshold ($\epsilon_e \leq \epsilon_e^{\text{thr}}$) and above-threshold ($\epsilon_e > \epsilon_e^{\text{thr}}$) regimes. The available experimental evidence on above-threshold SHI irradiation proves that neither the formation of the ion tracks nor the amorphization kinetics observed can be accounted for by the nuclear energy loss of the fast projectiles; instead, they have to be attributed to the high electronic energy deposition.^{3,4,8,9,11} Contrary, in the subthreshold regime the observed damage accumulation is largely due to the nuclear energy loss.¹¹

Further, the recent results of Wesch *et al.*^{7,8} and Kamarou *et al.*^{9,11} on the effects of SHI irradiation in virgin and pre-damaged InP show that, depending on the ion mass, ion energy, and irradiation temperature, SHI irradiation causes damage formation in virgin material and more or less notice-

TABLE I. SHI irradiation parameters [ion energy E_1 , ion specific energy E_1/M_1 (M_1 is the ion mass), ion initial charge q_{init} , ion equilibrium charge in the target bulk q_{mean} , range of ion fluences N_I , irradiation temperature T_I , electronic (ε_e) and nuclear (ε_n) ion energy loss at the surface, and number of vacancies per ion and unit path length N_v]. * symbols: q_{init} is expected to be close to q_{mean} . ε_e , ε_n , and N_v were calculated with the SRIM-2003 code³⁴ using a displacement energy E_d of 8.0 eV.³⁵

Ion	E_1 (MeV)	E_1/M_1 (MeV/u)	q_{init}	q_{mean}	N_I (cm ⁻²)	T_I	ε_e (keV/nm)	ε_n (keV/nm)	N_v (nm ⁻¹)
<i>Without Al foils</i>									
Kr	140	1.63	10	22.3	$(4 \times 10^{12}) - (2 \times 10^{15})$	RT	12.1	0.039	1.2
Xe	250	1.94	17	31.3	$(1 \times 10^{12}) - (1 \times 10^{14})$	RT	20.0	0.060	2.0
Xe	390	3.02	21	34.7	$(3 \times 10^{11}) - (3 \times 10^{14})$	LNT, RT	21.5	0.042	1.4
Au	593	3.01	30	46.3	$(7 \times 10^{10}) - (1 \times 10^{13})$	LNT, RT	29.1	0.078	2.5
<i>With Al foils</i>									
Xe	82	0.64	*	22.9	$(2 \times 10^{12}) - (1 \times 10^{14})$	RT	13.5	0.165	4.9
Xe	193	1.50	*	29.4	$(2 \times 10^{12}) - (3 \times 10^{13})$	RT	18.6	0.080	2.4
Au	64	0.32	*	23.0	$(5 \times 10^{11}) - (9 \times 10^{13})$	RT	10.7	0.568	15.2
Au	79	0.40	*	25.0	$(5 \times 10^{11}) - (9 \times 10^{13})$	RT	12.6	0.500	13.0
Au	150	0.76	*	31.3	$(2 \times 10^{11}) - (2 \times 10^{13})$	RT	18.8	0.259	7.5
Au	573	2.91	*	45.9	$(1 \times 10^{11}) - (5 \times 10^{12})$	RT	28.9	0.091	2.9

able damage annealing in predamaged material.

Generally, SHI irradiation of virgin InP in the electronic stopping regime causes the formation of small-size defects, i.e., simple point defects and point defect clusters. In addition to the simple defects mentioned above, more complex elongated defects such as ion tracks are formed due to high electronic energy loss ε_e in the *above-threshold electronic regime* (i.e., for SHI's with $\varepsilon_e > \varepsilon_e^{\text{thr}}$) and within a *limited range of irradiation temperatures*.³⁻⁶ The main points being discussed in the literature are the correlation between the number of ion tracks and the ion fluence in virgin and predamaged InP,^{3,4,10} the origin of discontinuous tracks,^{10,12,13} the wide distribution of track diameters,³ the influence of the irradiation temperature,^{4,5} and the internal structure of ion tracks in InP.^{3-5,10} It is worth mentioning that explanations, proposed by various authors on some of the points listed above, are sometimes mutually contradictory. Further, as was shown by us previously,⁹ the efficiency of damage formation and accumulation in InP cannot be explained solely by the linear energy transfer (LET) of the ion; the *radial distribution of the energy deposition*¹⁴ must also be taken into account. The last conclusion prejudices the amenity of a *single value* of the threshold LET $\varepsilon_e^{\text{thr}}$ as a fundamental quantity that is commonly used for description of track formation in solids irradiated with *different ion species*.

There are four main competing models of ion track formation due to high electronic energy deposition of SHI's in solids that are discussed in literature: Coulomb explosion,¹⁵⁻¹⁷ shock waves,¹⁸⁻²⁰ lattice relaxation,²¹⁻²³ and thermal spikes (TS).^{6,24,25} The TS model of track formation is a well established approach that has been successfully applied to some metals, intermetallic compounds, and dielectrics.²⁶⁻³⁰ Because of the complexity of all energy relaxation processes involved, this model is also subjected the same criticism³¹⁻³³ as the models mentioned above. However, the TS model seems to be the most elaborate one; furthermore, to our knowledge, currently it is the only model

able to provide at least approximate predictions on track formation in numerous conducting and nonconducting targets.

The purpose of the paper is to present our recent experimental results, and to show that they can be qualitatively and quantitatively explained using the thermal spike model. The results offer a self-consistent way to explain the influence of various irradiation conditions on the ion track formation and damage accumulation in InP and, therefore, can make a contribution to a better understanding of the underlying mechanisms.

II. EXPERIMENTS

We have used nominally undoped $\langle 100 \rangle \pm 0.5^\circ$ single-crystalline InP wafers. The wafers were cut into pieces (typically from 6×6 to 8×8 mm²). The samples were irradiated at the Hahn-Meitner Institute (Berlin, Germany) with 140 MeV Kr¹⁰⁺, 250 MeV Xe¹⁷⁺, 390 MeV Xe²¹⁺, or 593 MeV Au³⁰⁺ ions at room temperature (RT). A part of the InP samples was irradiated with 390 MeV Xe²¹⁺ or 593 MeV Au³⁰⁺ ions also at liquid nitrogen temperature (77 K, LNT) in order to examine a possible influence of the irradiation temperature. Additionally, thin aluminum (Al) foils with different thickness (from 0.8 μm to several tens of μm) were placed in front of some samples to obtain lower ion beam energies and, at the same time, to bring the projectiles into the mean equilibrium charge state (see Table I for details). Taking into account the experimental uncertainty of 0.5 μm in the thickness of the Al foils (excluding the 0.8- μm -thick one), the error in the energy estimation for, e.g., 64 or 79 MeV Au beams is ca. ± 7 MeV; this leads to a deviation of ± 0.8 keV/nm (i.e., $\pm 7\%$) in the value of electronic energy loss ε_e (from SRIM-2003 calculations). Ion beam scanning was used to irradiate the whole sample surface in a uniform way. In order to prevent heating of the samples during the SHI irradiations, the ion flux was kept low (at typically 1×10^{10} cm⁻² s⁻¹), and the samples were mounted to the

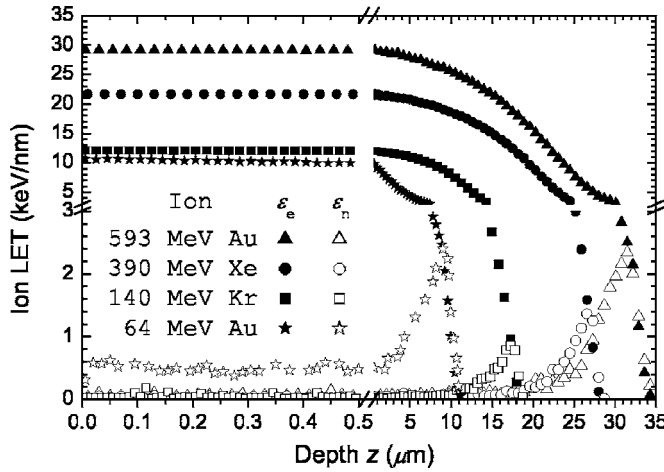


FIG. 1. Depth dependences of electronic and nuclear energy deposition for selected ion species (SRIM-2003 calculations). Note the breaks in both axes. In order to avoid overcrowding, the corresponding curves for other ion species are not shown here.

sample holder with silver paste giving a good thermal contact between them.

Figure 1 shows depth dependences of electronic (ϵ_e) and nuclear (ϵ_n) energy deposition for selected SHI species. One can see in Fig. 1 that for all ion species represented, the depth distributions of both ϵ_e and ϵ_n are almost uniform, and $\epsilon_e \gg \epsilon_n$ within the first $0.5 \mu\text{m}$ depth. This holds also for other ion species listed in Table I. Further, it is also clear from Table I and Fig. 1 that irradiations with SHI's decelerated by thin Al foils (excluding 193 MeV Xe and 573 MeV Au) are characterized by noticeably higher nuclear stopping than those in the first part of Table I (140 MeV Kr, 250/390 MeV Xe, and 593 MeV Au). Consequently, in the former case one can expect a larger influence of the nuclear energy deposition on the radiation damage formation.

The irradiated samples were analyzed by means of Rutherford backscattering spectrometry (RBS) in combination with the channeling technique using 1.4 MeV He ions at a laboratory scattering angle of 168° . This was done using the 3 MV Tandatron accelerator "JULIA" at the Institute of Solid State Physics of the Friedrich Schiller University (Jena, Germany). Under these conditions, the depth that can be analyzed in a quantitative manner in InP is approximately $0.6 \mu\text{m}$.

As a measure of the damage concentration within the irradiated layers, the difference in minimum yield $\Delta\chi_{\min}$ was taken. It is determined from the channeling spectra as a function of the depth z by

$$\Delta\chi_{\min}(z) = \frac{Y_{\text{aligned}}^{\text{irradiated}}(z) - Y_{\text{aligned}}^{\text{virgin}}(z)}{Y_{\text{random}}(z) - Y_{\text{aligned}}^{\text{virgin}}(z)},$$

where $Y_{\text{aligned}}^{\text{virgin}}(z)$ and $Y_{\text{aligned}}^{\text{irradiated}}(z)$ are the RBS yields of the aligned spectra (nonirradiated virgin and irradiated samples, respectively); $Y_{\text{random}}(z)$ is the yield measured in random direction. Assuming a random distribution of displaced lattice atoms within the lattice cell, the depth distributions of the relative concentration of displaced lattice atoms, $n_{\text{da}}(z)$, were

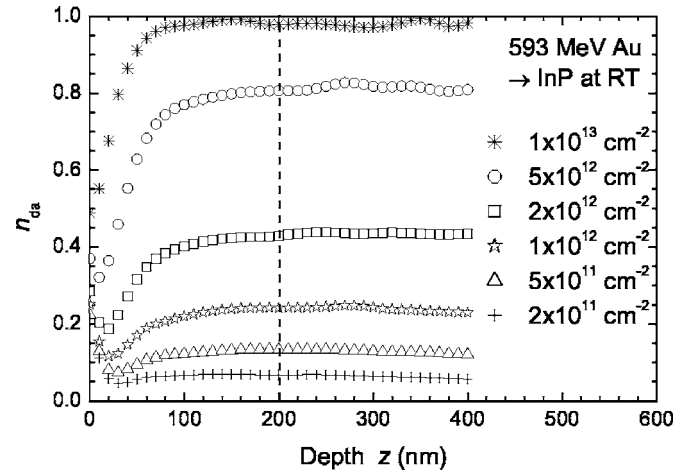


FIG. 2. Relative concentration of displaced lattice atoms vs depth, $n_{\text{da}}(z)$, in InP irradiated with different fluences of 593 MeV Au at RT. The vertical dashed line indicates the depth at which the data points shown in Fig. 4 were taken from.

calculated from the measured $\Delta\chi_{\min}(z)$ values. These calculations were performed using the DICADA code,³⁶ which is based on the discontinuous model of dechanneling. In the following, the relative concentration of displaced lattice atoms, n_{da} , is referred to as "damage concentration" for short. So, $n_{\text{da}}=0$ and $n_{\text{da}}=1$ correspond to undamaged virgin and to very heavily damaged (amorphized) material, respectively.

Further, some samples selected on the basis of the RBS results were additionally studied using transmission electron microscopy (TEM) in cross-section (X) and plan-view (PV) geometry. The thinned (electronically transparent) samples for PV-TEM were prepared by means of chemical etching performed either before SHI irradiations or after them. All the X-TEM samples were thinned down after SHI irradiations, using a mechanical polishing followed by a final ion beam milling. The TEM investigations were performed using either a Hitachi H-800 or a JEOL JEM-3010 instrument operating at 200 or 300 kV, respectively.

III. EXPERIMENTAL RESULTS

A. RBS results

Irradiation of virgin InP with SHI's in the above-threshold electronic regime causes lattice disordering up to amorphization.^{3,9,11} As an illustrative example, Fig. 2 shows the depth dependence of the damage concentration, n_{da} , formed by 593 MeV Au at RT for various ion fluences. One can see that the Au irradiation causes material damaging up to amorphization. Further, in depths behind an only slightly damaged surface layer the damage concentration remains almost constant, which is in accordance with the uniformity of the depth distributions of both electronic and nuclear energy deposition (see Fig. 1).

However, unlike the bulk, a thin surface layer (tens of nanometers) remains almost undamaged, as it is shown in Fig. 2. This is also the case for 250 and 390 MeV Xe irradiations provided that the initial ion charge is noticeably

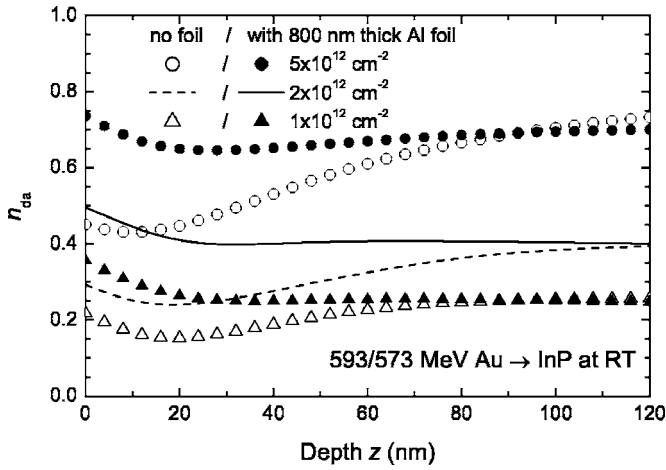


FIG. 3. Depth distributions of n_{da} (from RBS measurements) for three different fluences of 593 MeV Au. The corresponding pairs of curves make it possible to compare the efficiency of damage formation within the first tens of nm, which results from either 593 MeV Au³⁰⁺ ions or the same beam but passed through 0.8- μ m-thick Al foil. In the former case, the initial ion charge is noticeably lower than the equilibrium one in the bulk, while in the latter case it is expected to be close to the equilibrium charge of the ion. The small peaks at $z=0$ are merely due to surface peaks that are unavoidable in aligned RBS spectra.

lower than the mean equilibrium one in the target bulk (see Table I).¹¹ Conversely, this effect should not take place if the initial ion charge is close to the equilibrium one in the bulk. In order to verify this, we performed irradiations of InP with 593 MeV Au³⁰⁺ ions passed through a thin (0.8 μ m) Al foil. In this way, the ion beam energy is lowered by 20 MeV and, simultaneously, the charge of the ions is increased up to its equilibrium value, specific for the Al bulk. So as the projectile charge is only very weakly dependent on the properties of the solid target,³⁷ the charge of 573 MeV Au ions just before entering InP is expected to be very close to the equilibrium one in bulk InP. Figure 3 shows depth distributions of damage formed by a direct 593 MeV Au³⁰⁺ irradiation, on the one hand, and by an irradiation after the beam passed through the 0.8 μ m thick Al foil, on the other hand. We can see in the figure that the $n_{da}(z)$ profiles for (573 MeV Au) irradiations through the foil are uniform and do not show the decrease in n_{da} close to the surface, occurring for the direct irradiations (see also Fig. 2). This experimental result clearly shows that the noticeably lower efficiency of damage formation at the surface is explained solely by the initial ion charge being lower than the equilibrium one in the bulk (for details, see Ref. 11).

Figure 4 summarizes the corresponding fluence dependence of n_{da} (the data points are taken from the depth of 200 nm as indicated by the vertical dashed line in Fig. 2) for all ion species and experimental conditions presented in Table I. More detailed information about the process of defect formation can be obtained by analyzing the ion fluence dependence of n_{da} in the framework of the overlap damage model introduced by Gibbons.³⁸ In this model it is assumed that amorphous material is produced either directly by a single incoming ion or by multiple overlap of damaged but

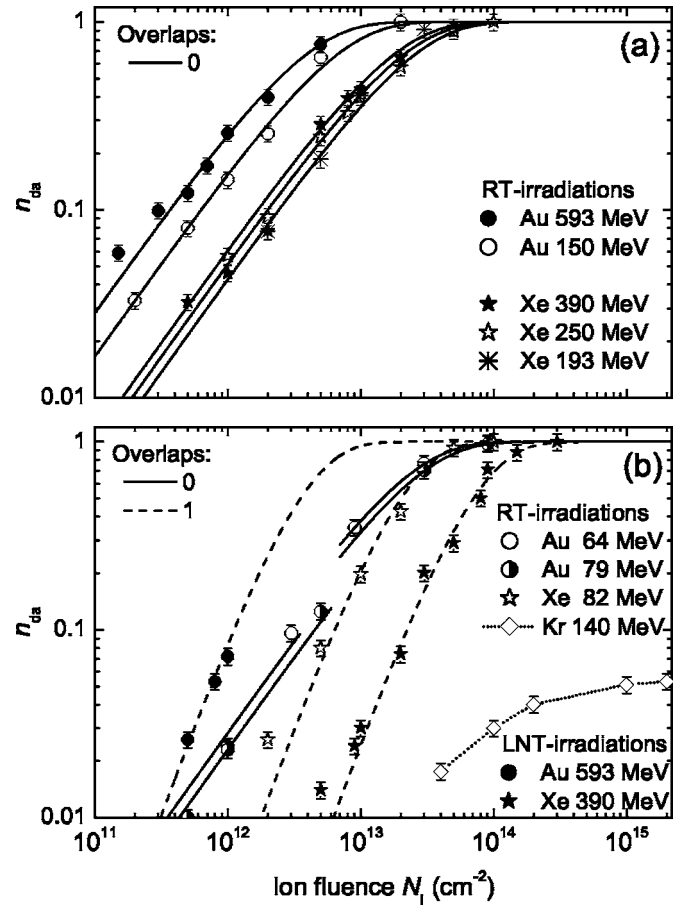


FIG. 4. Relative concentration of displaced lattice atoms vs the ion fluence for different ion species listed in Table I. In order to avoid the effect of the initial ion charge presented in Fig. 3, the data points are taken at the depth of 200 nm (see Fig. 2). Parts (a) and (b) cover all above-threshold and subthreshold irradiations, respectively (see Introduction and Discussion). The relative error of the ion fluence values is about 10% and, hence, is well represented by the data point sizes. The dotted line connecting the data points for 140 MeV Kr in (b) is only to guide the eye. Solid and dashed lines in both parts stand for fitting curves obtained by using Gibbons' overlap damage model assuming zero or first order of overlapping, respectively.

not amorphized areas. The fitting of the fluence dependences within this model yields the number m of overlaps necessary to amorphize the material, and the area A_l damaged by a single ion (damage cross section). Obviously, for all above-threshold RT irradiations with different ion species and beam energies, the fluence dependences can be fitted with an overlap number $m=0$ [see Fig. 4(a)]. This means that each single ion creates a heavily damaged area along its trajectory directly. Conversely, the assumption of one overlap is necessary to fit the experimental curves in the case of irradiations with 82 MeV Xe at RT and all LNT irradiations (390 MeV Xe and 593 MeV Au), as can be seen in Fig. 4(b). It should be mentioned that only three data points for LNT irradiation of InP with 593 MeV Au are shown in Fig. 4(b). Unfortunately, no further points can be presented, because larger fluences of Au cause sample breaking at LNT. Nevertheless, the initial build-up of the radiation damage is well repre-

TABLE II. Number of overlaps m , damage cross sections A_I , and resulting radii $r_{\text{RBS}} = \sqrt{A_I/\pi}$ obtained from Gibbons' model for different SHI irradiations of InP.

Ion	E_1 (MeV)	E_1/M_1 (MeV/u)	T_I	m	A_I (nm ²)	r_{RBS} (nm)
Xe	193	1.50	RT	0	4.3 ± 0.4	1.2 ± 0.1
Xe	250	1.94	RT	0	5.3 ± 0.5	1.3 ± 0.1
Xe	390	3.02	RT	0	6.3 ± 0.6	1.4 ± 0.1
Au	150	0.76	RT	0	16.7 ± 1.7	2.3 ± 0.1
Au	593	3.01	RT	0	28.6 ± 2.9	3.0 ± 0.2
Xe	82	0.64	RT	1	8.3 ± 0.8	1.6 ± 0.1
Xe	390	3.02	LNT	1	2.4 ± 0.2	0.9 ± 0.1
Au	593	3.01	LNT	1	47.6 ± 4.8	3.9 ± 0.2
Kr	140	1.63	RT			
Au	64	0.32	RT	0	4.8 ± 0.5	1.2 ± 0.1
Au	79	0.40	RT	0	4.0 ± 0.4	1.1 ± 0.1

sented and is in agreement with that of 390 MeV Xe at LNT [see Fig. 4(b)]. 140 MeV Kr irradiation does not lead to amorphization, and the n_{da} value at the maximum ion fluence equals 0.05, i.e., only 5% of the target atoms are displaced from their regular lattice positions. Finally, the data points for 64/79 MeV Au irradiations cannot be fitted by single curves assuming any integer value of m . Nevertheless, in both cases the data points for $n_{\text{da}} \leq 0.1$ and $n_{\text{da}} > 0.1$ can be separately fitted by curves with $m=0$, but with different damage cross sections A_I (for $n_{\text{da}} \leq 0.1$: 2.9 and 2.3 nm² for 64/79 MeV Au, respectively; and for $n_{\text{da}} > 0.1$: 4.8 and 4.0 nm² for 64/79 MeV Au, respectively). The values of the damage cross sections A_I and number of overlaps m obtained from Gibbons' model for different ion species and energies are summarized in Table II. However, it should be kept in mind that those calculated damage cross sections for all SHI species are *mean values* of the damage areas (produced per ion) that can be different in size (see discussion in Sec. VIII B).

B. TEM results

It is known that defects can be annealed under irradiation with energetic electrons during TEM analysis. Generally, ion tracks are not stable under the electron beam during TEM analysis. As an example, Fig. 5 shows a series of PV-TEM images of an InP sample irradiated with 593 MeV Au at RT. One can see that already after the first 3 min the TEM image changes very noticeably. Unfortunately, the damage zones (especially the smallest ones) shrink very fast and, therefore, we were not able to obtain high (atomic) resolution TEM images that could reveal the *original* inner structure of the observed ion tracks.

A similar effect of recrystallization was also reported by Jenčič *et al.* during TEM observations of amorphous zones formed by room-temperature irradiation of InP with 50–300 keV Xe ions.³⁹

Figures 6(a) and 6(b) show X-TEM images of an InP sample irradiated with 593 MeV Au at RT. The first one is taken at a depth of ca. 5–6 μm , where ε_e is still very high

and, hence, continuous tracks are formed. The second part of the figure shows the interval where rather continuous tracks are first substituted by discontinuous ones, and then, gradually, no tracks are visible with increasing depth.

In order to estimate the number of visible ion tracks, PV-TEM images are used commonly. As an example, Fig. 7 demonstrates a plan-view TEM image of an InP sample irradiated at RT with a relatively low ion fluence of 573 MeV Au ions.⁴⁰

Finally, Fig. 8 shows discontinuous tracks formed by LNT irradiations with 390 MeV Xe. The ion tracks are observed as strings of dots or short (up to ca. 100 nm length) lines. The main results obtained by TEM studies are summarized in Table III.^{40,41}

IV. THEORETICAL BACKGROUND

In the following we will consider SHI bombardment of surfaces of solid semiconductors. The corresponding energy loss per unit path length of a SHI with the atomic number Z_1 , energy E_1 , and mass M_1 can be divided into two parts: nuclear (ε_n) and electronic energy loss (ε_e). It was shown that the high electronic energy deposition of SHI-bombarded InP samples forms measurable damage in the near-surface

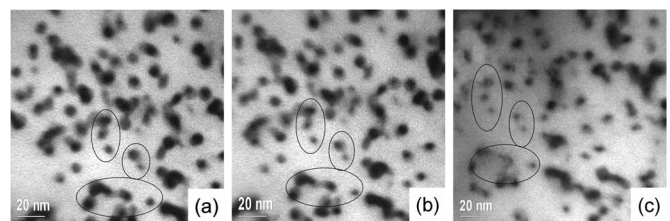


FIG. 5. PV-TEM images of an InP sample irradiated with 593 MeV Au at RT. The series of images illustrates the temporal evolution of single and overlapping ion tracks under TEM electron beam. The TEM observations were performed at RT. Part (a) shows the initial picture, while (b) and (c) are after 2 and 3 min, respectively.

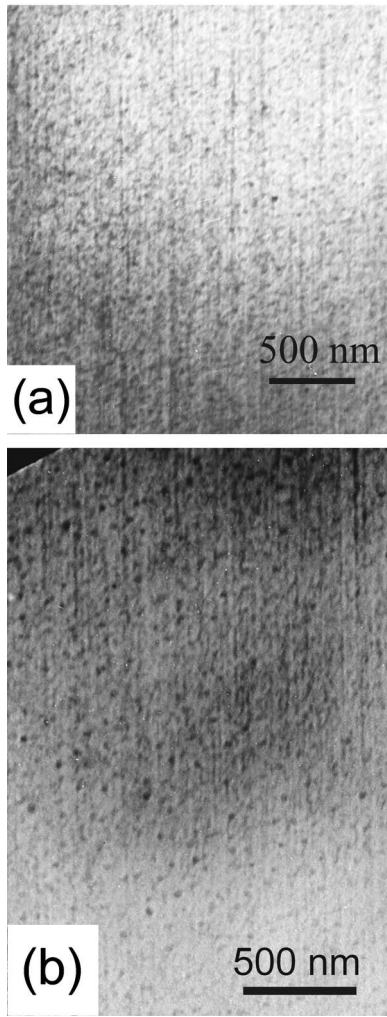


FIG. 6. X-TEM images of an InP sample irradiated with 593 MeV Au at RT. The ion fluence is $2 \times 10^{12} \text{ cm}^{-2}$ and the corresponding value of n_{da} is 40% as follows from RBS measurements [see Fig. 4(a)]. Parts (a) and (b) correspond to depths of about 5–6 and 25–30 μm , respectively. The first part demonstrates continuous tracks, while the second one shows three different depth intervals containing rather continuous tracks, discontinuous tracks, and no tracks, respectively. The direction of ion movement in (a) and (b) is from top to bottom.

region. The question is how this high amount of electronic excitation is transferred into atomic motion.

The initial processes of the energy transfer from a SHI take only 10^{-19} – 10^{-17} s for inner-shell interactions and slightly longer (about 10^{-16} s) for collective electronic excitations (formation of plasmons).³⁷ Hence, just after the passage of the SHI, the narrow cylindrical target zone coaxial with the SHI path consists of a two-component plasma of “cold” lattice atoms and “hot” electrons. Such a narrow region is often called “ionization spike.” The initial energy distribution and dynamics of the hot charge carriers within “ionization spikes” have been extensively studied by Schiwietz *et al.* by means of Auger-electron spectroscopy.⁴² Irradiation of matter by ultrashort (fs, ps, or ns scale) laser pulses is one more powerful technique widely used to study the ultrafast dynamics of the excited charge carriers and the energy

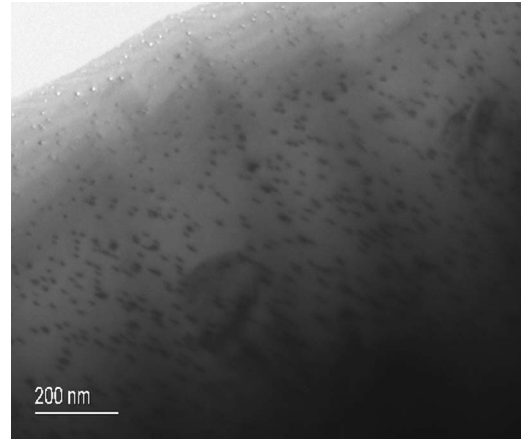


FIG. 7. PV-TEM image of an InP sample irradiated at RT with a relatively low fluence ($1 \times 10^{11} \text{ cm}^{-2}$) of 573 MeV Au ions. In this case, the number of ion tracks is $\geq 9 \times 10^{10} \text{ cm}^{-2}$. Taking into account the experimental error for the estimation of the ion fluence ($\pm 10\%$), one can conclude that each 573-MeV Au ion produces a visible track.

transfer to the lattice from the temporal evolution of the optical properties of the material.^{43–45} The principal difference between plasmas formed by SHI’s and by laser irradiation of solids is the energy distribution of freed electrons. Laser pulses lead to an almost uniform energy distribution (i.e., each loosely bound and freed electron gains approximately equal energy defined by the laser wavelength). Conversely, electrons located close to the paths of the SHI’s gain very different energies depending on their binding energy and impact parameter. Therefore, the second stage of energy transfer and redistribution within ionization spikes (stage of electronic energy thermalization) is meaningful only for SHI irradiations, but not for laser ones.

In the following, the first stage of energy relaxation (i.e., ionization spikes formed by SHI’s) will be considered in more detail. In order to do so, one faces the following basic aspects: the number of electrons freed from their host atoms, their initial energy distribution, and their initial radial distribution.

The energy distribution and number of freed electrons per unit path length can be obtained from the classical Rutherford formula⁴⁶ for δ -ray production by a single ion,

$$\frac{dn}{d\varepsilon} = \frac{4\pi N_{e,b}^{(I)} Z_{\text{eff}}^2 e^4}{\varepsilon_{\text{max}}} \frac{1}{(\varepsilon + I)^2} = \frac{\psi}{(\varepsilon + I)^2}, \quad \text{where}$$

$$\psi = \frac{4\pi N_{e,b}^{(I)} Z_{\text{eff}}^2 e^4}{\varepsilon_{\text{max}}}. \quad (1)$$

Here dn is the number of freed electrons within the energy interval $(\varepsilon, \varepsilon + d\varepsilon)$, Z_{eff} is the effective charge number of the ion ($=Z_1$ for bare ions; otherwise it can be calculated using formulas given, e.g., in the reviews by Betz⁴⁷ or Ahlen⁴⁸), $e = e_0 / \sqrt{4\pi\varepsilon_0}$ (e_0 is the electron charge and ε_0 is the vacuum permittivity), and $N_{e,b}^{(I)}$ is the volume concentration of electrons bound with energy I to the atoms. ε_{max} is the maximum energy that can be transferred to an electron in a single col-

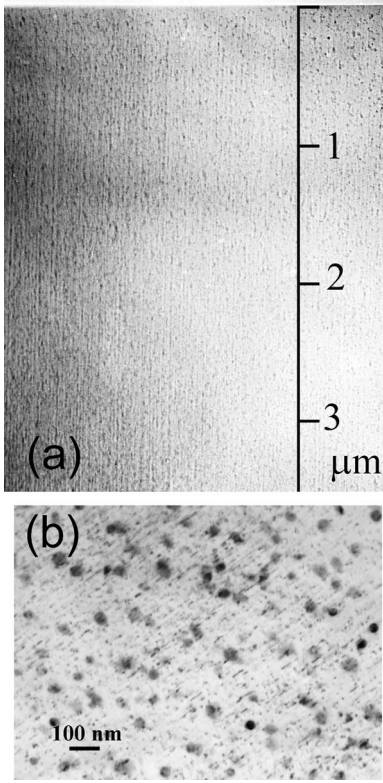


FIG. 8. (a) Low-magnification X-TEM image of an InP sample irradiated with 390 MeV Xe at LNT. The ion fluence is $3 \times 10^{13} \text{ cm}^{-2}$ and the corresponding value of n_{da} is 20% as it follows from RBS measurements [cf. Fig. 4(b)]. One can see discontinuous tracks visible as dark interrupting lines. (b) Image of the same sample as in (a), but shown with a higher magnification, and taken at a depth of about 3–5 μm . Discontinuous tracks are clearly visible as either short continuous dark lines or strings of dark points. Larger round-shaped gray or black spots with diameters of 30–45 nm are small In droplets located on the TEM sample surface, which are formed during the ion-beam milling procedure.

lision with $\varepsilon_{\text{max}} = 2m_e \gamma^2 \beta^2 c^2$. Here m_e is the electron mass, $\gamma^2 = 1/(1 - \beta^2)$, and $\beta = v/c$, where v is the ion velocity and c is the speed of light in vacuum.

As it was suggested by Sigmund *et al.*,⁴⁹ any use of the effective charge is discouraged below the screening limit of $0.025Z_1^{4/3} \text{ MeV/u}$. For the used ion species Kr, Xe, and Au, this yields 2.97, 5.10, and 8.47 MeV/u, respectively. Hence, for all performed SHI irradiations (Table I) the specific ion energies are below the screening limit mentioned above. Therefore, Z_{eff} and, consequently, ψ are treated as unknown parameters for all performed SHI irradiations.

Assuming an average binding energy \bar{I} , the total number and the total energy of the electrons freed by a single ion per unit path length can be calculated from Eq. (1),

$$\Delta N = \int_0^{\varepsilon_{\text{max}}} \frac{dn}{d\varepsilon} d\varepsilon = \psi \frac{1}{\bar{I}(1+k)},$$

$$\Delta E = \int_0^{\varepsilon_{\text{max}}} \varepsilon \frac{dn}{d\varepsilon} d\varepsilon = \psi \left[\ln \left(1 + \frac{1}{k} \right) - \frac{1}{1+k} \right], \quad (2)$$

where $k = \bar{I}/\varepsilon_{\text{max}}$. Hence, the mean value and the standard deviation of the energy per electron are given by

$$\bar{\varepsilon} = \frac{\Delta E}{\Delta N} = \bar{I} \left[(1+k) \ln \left(1 + \frac{1}{k} \right) - 1 \right],$$

$$\sigma = \sqrt{\overline{\varepsilon^2} - \bar{\varepsilon}^2} = \bar{I} \sqrt{\left(1 + \frac{1}{k} \right) - \left[(1+k) \ln \left(1 + \frac{1}{k} \right) \right]^2}. \quad (3)$$

Using the recommended mean binding energies of 481 eV for In atoms and 172 eV for P atoms,⁴⁸ the calculations yield, for the example of 150 MeV Au, $\bar{\varepsilon} \approx 450 \text{ eV}$, $\sigma \approx 420 \text{ eV}$, and $\bar{\varepsilon} \approx 280 \text{ eV}$, $\sigma \approx 340 \text{ eV}$ for the In and P sublattices of the target, respectively. Generally, the mean value of the energy per freed electron increases with increasing specific energy of the ion and varies from ca. 250 to 910 eV for In target atoms and from 180 to 480 eV for P atoms for the performed SHI irradiations.

In order to analyze the basic energy distribution [Eq. (1)], it is useful to introduce the functions

$$f_n(\varepsilon) = \frac{1}{\Delta N} \int_0^{\varepsilon} \frac{dn}{d\varepsilon} d\varepsilon = \frac{1 + \bar{I}/\varepsilon_{\text{max}}}{1 + \bar{I}/\varepsilon},$$

$$f_\varepsilon(\varepsilon) = \frac{1}{\Delta E} \int_0^{\varepsilon} \varepsilon \frac{dn}{d\varepsilon} d\varepsilon = \frac{\ln(1 + \varepsilon/\bar{I}) - (1 + \bar{I}/\varepsilon)^{-1}}{\ln(1 + \varepsilon_{\text{max}}/\bar{I}) - (1 + \bar{I}/\varepsilon_{\text{max}})^{-1}}. \quad (4)$$

Here $f_n(\varepsilon)$ is the number of electrons (per unit path length) freed by a single ion and having energies within the interval $(0, \varepsilon)$ relative to their total number ΔN per unit path length. The second function in Eqs. (4), $f_\varepsilon(\varepsilon)$, stands for the energy (per unit path length) that is accumulated by all electrons within the energy interval $(0, \varepsilon)$ relative to the total electronic energy ΔE per unit path length. The expressions for ΔN and ΔE are given in Eqs. (2). Obviously, both functions in Eqs. (4) depend only on the mean binding energy \bar{I} (target property) and on the maximum electron energy ε_{max} (ion property). The latter value, in turn, depends only on the ion velocity (see above). Consequently, different SHI's having almost equal specific energy E_1/M_1 (such as 390 MeV Xe and 593 MeV Au, see Table I) will be represented by virtually the same $f_n(\varepsilon)$ and $f_\varepsilon(\varepsilon)$ functions. The energy distributions given in Eqs. (4) are illustrated in Fig. 9 for selected ion species. One can see in Fig. 9(a) that the fraction of electrons with an energy of $\varepsilon \leq 10 \text{ eV}$ is about 2–6 %, and their total energy is in all cases less than 1% of the ion energy loss [see Fig. 9(b)]. The fraction of electrons within the energy range of 10–100 eV varies between 15% and 40%, and their total energy is limited to 10% in the maximum. Conversely, very fast electrons (for $\varepsilon \geq 1 \text{ keV}$) can constitute 25% of the total freed electrons but can carry up to 75% of the total energy lost by the ions. Finally, a major part of the electrons belongs to an intermediate energy range

TABLE III. Summary of TEM results.

Ion	E_1 (MeV)	N_I (cm ⁻²)	T_I	X- or PV- TEM	Number of tracks ^a (cm ⁻²)	Track radii ^b r_{TEM} (nm)
Xe	250	3×10^{12}	RT	PV	$> 1.0 \times 10^{11}$	2.2–4.0
Xe	250	5×10^{12}	RT	PV	$> 1.4 \times 10^{11}$	2.2–4.0
Xe	390	3×10^{13}	LNT	X		1.5–3.0
Au	150	5×10^{11}	RT	PV	$> 1.0 \times 10^{11}$	2.0–3.5
Au	573	1×10^{11}	RT	PV	$> 9.0 \times 10^{10}$	1.7–3.5
Au	593	5×10^{11}	RT	PV	$> 2.0 \times 10^{11}$	1.5–4.5
Au	593	7×10^{11}	RT	PV	$> 2.5 \times 10^{11}$	1.5–4.5
Au	593	9×10^{11}	RT	PV	$> 3.5 \times 10^{11}$	1.5–4.5
Au	593	1×10^{12}	RT	X		2.0–4.5
Au	593	2×10^{12}	RT	X		2.0–4.5

^aReference 40.^bReference 41.

from 100 eV to 1 keV [cf. also with the mean energies of the electrons obtained from Eqs. (3)] and share from 25% to 90% of the total electronic energy depending on the SHI velocity.

In order to calculate the projected ranges r_p of the energetic electrons escaping from the initial ionization spikes, we have used the CASINO Monte Carlo code⁵⁰ (version 2.42). As an illustrative example, Fig. 10 shows the range distributions of 200 eV, 500 eV, 1 keV, and 2 keV electrons in InP. One can see that the mean projected range of such electrons varies from units to tens of nanometers.

It should be mentioned that the basic Eq. (1) supposes that all (initially bound) electrons have equal binding energy I . In practice, however, the electron binding energies in the outermost and the innermost electronic shells of heavy atoms (e.g., In) can differ by three to four orders of magnitude. Nevertheless, expression (1) holds for any specific electronic shell and can be applied for practical calculations providing that absolute or relative ionization cross sections are known for each electronic shell. Such cross sections were calculated using the CASP code by Grande and Schiwietz.⁵¹ The results of the corresponding CASP calculations show that most of the

SHI energy is transferred to outer electronic shells. So as fast ions are decelerated mainly through ionization of target atoms and much less through excitation of valence- and conduction-band states,³⁷ we can neglect excitation events and consider the cross sections Q_e calculated by the CASP code as related only to ionization energy losses that are caused by SHI interaction with each specific electronic shell of the target atoms. Consequently, the ΔE value in Eqs. (2) can be substituted by the corresponding partial energy loss of the ion due to interaction with the i th shell,

$$\varepsilon_e^{(i)} = \frac{Q_e^{(i)}}{\sum_k Q_e^{(k)}} \varepsilon_e, \quad (5)$$

where ε_e is the total energy loss of the ion per unit path length. The performed substitution allows calculating the term ψ from the last expression⁵² in Eqs. (2) and put it into the first expression. In this way one obtains the number of electrons detached from each specific shell $\Delta N^{(i)}$. Finally, the summation over all electronic shells of the two atom species

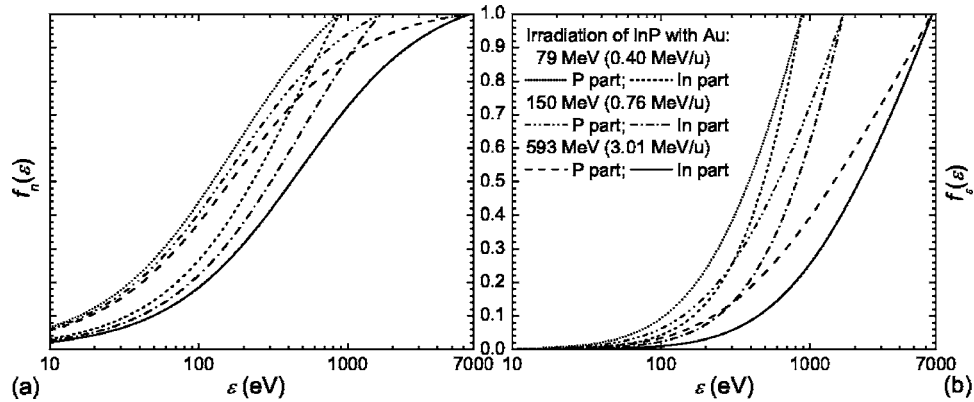


FIG. 9. Auxiliary functions $f_n(\varepsilon)$ (a) and $f_\varepsilon(\varepsilon)$ (b) given by Eqs. (4), for different representative SHI irradiations. The former function stands for the number of electrons (per unit path length) freed by a single ion and having energies within the interval $(0, \varepsilon)$ relative to their total number per ion and unit path length. The latter function represents the energy (per unit path length) that is accumulated by all electrons within the energy interval $(0, \varepsilon)$ relative to the total electronic energy per ion and unit path length. The description given in (b) is valid for (a) as well.

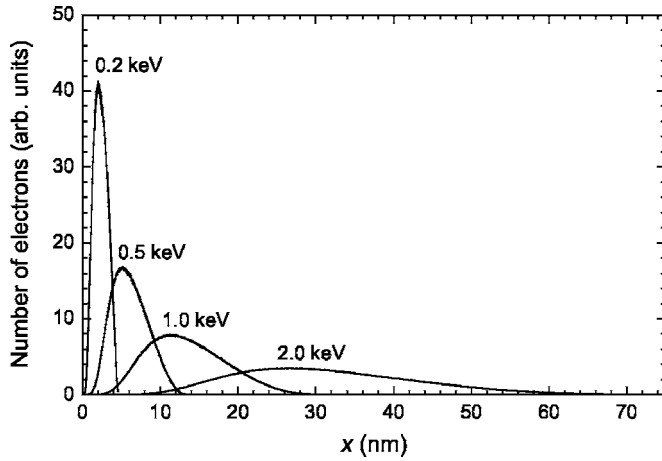


FIG. 10. Range distribution of electrons with initial energy of 200 eV, 500 eV, 1 keV, and 2 keV in InP as calculated by the CASINO code (Ref. 50).

provides the total number of freed electrons $N_e^{(\text{total})}$ per unit path length.

In the next step the initial radial distribution of electrons detached by a single SHI from their host atoms is considered. The formula for the impact parameter (r) dependent ion energy loss⁵³ in a single collision of an ion with an electron can be rewritten as

$$\varepsilon(r) = \frac{(b_e/2)^2}{(b_e/2)^2 + r^2} \varepsilon_{\text{max}} \quad (6)$$

with

$$b_e = \frac{Z_1 e_0^2}{4\pi\epsilon_0 E_1} \frac{1}{m_e}.$$

From this one obtains an impact-parameter-dependent energy transfer to a single electron (i.e., the initial radial distribution) in the approximation of the free electron gas according to

$$\varepsilon(r) = \frac{\varepsilon_{\text{max}}}{1 + \chi^2 r^2}, \quad \text{where } \chi = \frac{4\pi\epsilon_0 m_e v^2}{Z_1 e_0^2} = \frac{2\pi\epsilon_0 \varepsilon_{\text{max}}}{Z_1 e_0^2}. \quad (7)$$

For nonbare ions the charge Z_1 of the nucleus must be replaced with their ionization degree q . The last equation allows one to calculate the maximum distance at which an electron in the outermost electronic shell of a target atom can be detached from its host atom (this distance is limited by the target energy gap E_g),

$$r_{\text{max}} = \frac{1}{\chi} \sqrt{\left(\frac{\varepsilon_{\text{max}}}{E_g} - 1\right)}. \quad (8)$$

The ionization degree q of the ion is calculated using formulas for the mean equilibrium charge state \bar{q} of the ion that are given by Schiwietz *et al.*³⁷ The calculations yield, for the example of 250 MeV Xe, $r_{\text{max}} \cong 1$ nm and $N_e^{(\text{total})} = 189 \text{ nm}^{-1}$. Therefore, the initial density of detached elec-

trons is of the order of $6 \times 10^{22} \text{ cm}^{-3}$ and is comparable with the atomic density of InP ($3.96 \times 10^{22} \text{ cm}^{-3}$).

Now the temporal evolution of the ionization spikes will be considered. Unfortunately, unlike the initial stage of the formation of the ionization spikes, the cooling stage is not so well studied. First, the differently hot carriers redistribute energy among themselves (electronic energy thermalization). Second, they transfer some part of the energy to the surrounding cold lattice (e.g., due to the carrier-optical phonon scattering,⁵⁴ which is the main mechanism for compound semiconductors consisting of light and heavy constituents). Finally, the highly excited nonequilibrium carriers in the electron-hole plasma can recombine or be scattered by ionized impurities,⁵⁵ though at room temperature and at elevated temperatures the last two mechanisms are much slower than the carrier-carrier and carrier-phonon scattering processes mentioned above.^{33,43,55,56} Hence, the initial stage of electronic energy thermalization is followed by a relaxation stage, where the hot carriers exchange energy with the lattice by emission and absorption of phonons, which results in a net flow of energy from the carriers to the lattice (so-called “electron-phonon coupling”). It should be mentioned that some part of nonequilibrium phonons emitted in earlier events will be reabsorbed by the charge carriers, which slows down the overall cooling process to some extent.⁵⁶

V. MODELING OF THERMAL SPIKES

The theoretical simulations have been performed on the basis of coupled differential equations of heat flow both in the electron gas and the atomic lattice (see, e.g., Toulemonde *et al.*²⁴),

$$C_e(T_e) \frac{\partial T_e}{\partial t} = \frac{1}{r} \frac{\partial}{\partial r} \left[r K_e(T_e) \frac{\partial T_e}{\partial r} \right] - g(T_e - T_a) + A(r, t),$$

$$C_a(T_a) \frac{\partial T_a}{\partial t} = \frac{1}{r} \frac{\partial}{\partial r} \left[r K_a(T_a) \frac{\partial T_a}{\partial r} \right] + g(T_e - T_a), \quad (9)$$

where C_e, K_e and C_a, K_a are the specific heat and thermal conductivity of electrons and atoms, respectively; T_e and T_a are the electronic and atomic temperature (average energy); r is the radial distance from an ion trajectory; t is the time; g is the efficiency of the energy transfer from excited electrons to the lattice (so-called electron-phonon coupling); and A is the energy density²⁶ deposited in target electrons,

$$A(r, t) = \alpha \exp\left(-\frac{(t - t_0)^2}{2t_0^2}\right) F(r), \quad (10)$$

where α is a normalization constant and t_0 is the energy deposition time (time necessary to slow down fast electrons).³⁰

As is known from many experiments on ion irradiation of different targets, visible tracks consist of two distinct zones.^{57–59} The maximum track radius r_p is determined by the range of the most energetic electrons produced by the ions (see Sec. IV and Fig. 10). Such a wide cylindrical zone of a track is called “ultrack,” “halo,” or “penumbra.” A much thinner cylindrical zone of primary ionization with a

radius $r_c = r_{\max}$ [see Eq. (8)] is called “infratrack” or “core.” The average accumulated dose within the track core is usually orders of magnitude higher than that in the track penumbra.

Chatterjee and Schaefer⁵⁷ have proposed the following expressions for the average initial energy densities in the ion track as functions of the radial distance r from the ion path:

$$\rho_c = \frac{\varepsilon_e}{2\pi r_c^2} \left[1 + \frac{1}{2 \ln(e^{1/2} r_p / r_c)} \right] \text{ for } r \leq r_c,$$

$$\rho_p(r) = \frac{\varepsilon_e}{4\pi r^2 \ln(e^{1/2} r_p / r_c)} \text{ for } r_c < r \leq r_p. \quad (11)$$

The densities mentioned above are semiempirical (the r^{-2} distribution comes from experiments), self-consistent (they are monotonous and finite), and (as can be easily proven) self-normalized, i.e., $\int_0^{r_c} \rho_c 2\pi r dr + \int_{r_c}^{r_p} \rho_p 2\pi r dr = \varepsilon_e$ is valid. Therefore, we can write

$$F(r) = \rho_c + \rho_p(r). \quad (12)$$

The constant α in Eq. (10) can be calculated from the normalization condition for the initial energy density $A(r, t)$ by

$$\int_{t=0}^{\infty} \int_{r=0}^{r_p} A(r, t) 2\pi r dr dt = \varepsilon_e. \quad (13)$$

As was already mentioned, the spatial term of $A(r, t)$ [i.e., $F(r)$ in Eq. (10)] is self-normalized. The integration of the time-dependent term of $A(r, t)$ yields

$$\int_0^{\infty} e^{-(t-t_0)^2/2t_0^2} dt = t_0 \sqrt{2} \int_{1/\sqrt{2}}^{\infty} e^{-x^2} dx = t_0 \sqrt{\frac{\pi}{2}} \operatorname{erfc}\left(\sqrt{\frac{1}{2}}\right) \cong 0.398 t_0. \quad (14)$$

As a consequence of Eq. (14), α is given by

$$\alpha \cong (0.398 t_0)^{-1}. \quad (15)$$

Further, in accord with the initial distribution of the energy density [see Eqs. (11)], the radial distribution of the free electron concentration $n_e(r)$ is given by

$$n_e(r) = \begin{cases} \frac{N^*}{\pi r_c^2} & \text{for } r \leq r_c \\ \frac{N^*}{\pi r^2} e^{1-r/r_c} & \text{for } r_c \leq r \leq r_p, \end{cases} \quad (16)$$

where N^* is a normalization constant that is determined from $\int_0^{r_p} n_e(r) 2\pi r dr = N_e^{(\text{total})}$ with $N_e^{(\text{total})}$ being the total number of freed electrons per ion and unit path length (it is calculated as described in Sec. IV).

The electron-phonon coupling efficiency²⁹

$$g = \frac{\pi^2 m_e n_e v_s^2}{6 \tau_e (T_e) T_e} \quad (17)$$

was introduced originally for metals.⁶⁰ Here n_e is the volume concentration of free electrons, v_s is the sound velocity, and $\tau_e(T_e)$ is the mean free time between two collisions of an

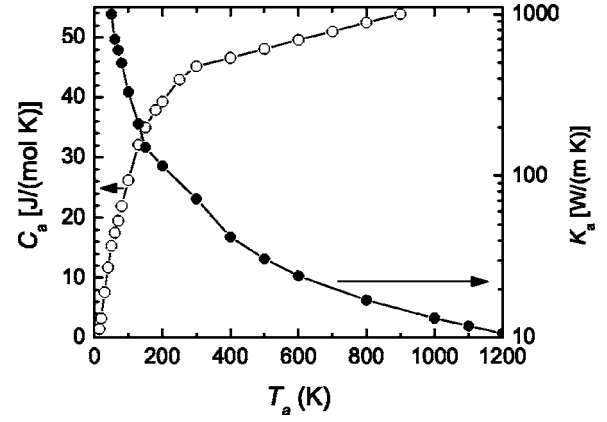


FIG. 11. Temperature dependence of the specific heat C_a and thermal conductivity K_a of the lattice (open and closed symbols, respectively). The data points are from Refs. 62 and 63. To our knowledge, there are no data in the literature on the thermal properties of InP for higher temperatures; therefore, the presented curves are extrapolated additionally.

electron at the temperature T_e .²⁹ However, as is known from laser experiments on the temporal evolution of the optical properties of various semiconductors,^{44,45} the energy gap closes and one observes a metallic behavior if about 10% of the valence electrons are excited to the conduction band. As was shown above, this condition holds in the wake of a SHI, that is, close to the ion path. Further, as was suggested by other authors, hot electrons in the conduction band of non-metallic solids will behave like hot electrons in a metal.^{30,61} Therefore, Eq. (17) will be used in this study as well.

VI. DATA USED FOR THE CALCULATIONS

The $C_e(T_e)$ and $K_e(T_e)$ dependences are not known for InP. Therefore, it was assumed that freed electrons with high energies can be considered as quasifree particles (see above). Consequently, the specific heat and the thermal conductivity of the electrons are taken to be

$$C_e = \frac{3}{2} k_B n_e,$$

$$K_e = C_e D_e, \quad (18)$$

where k_B is the Boltzmann constant and D_e is the thermal diffusivity of the electrons that is taken to be $5 \text{ cm}^2/\text{s}$ close to the value used by Meftah *et al.*³⁰ for yttrium iron garnet. The temperature dependences of C_a and K_a taken from Refs. 62 and 63 are shown in Fig. 11. The value of the average sound velocity $v_s = 5130 \text{ m/s}$ is from Ref. 64. The parameter t_0 in Eq. (10) was taken to be $5 \times 10^{-15} \text{ s}$. Izui⁶⁵ suggested that the energy is shared between electrons within ca. $1 \times 10^{-15} \text{ s}$. However, a variation of this term within $(1-5) \times 10^{-15} \text{ s}$ has almost no influence on the results of the calculations.⁶⁶ Conversely, the parameter τ_e strongly influences the results of the calculations and cannot be taken arbitrarily. Instead, τ_e must be estimated from available experimental data. To do so, we have used the data on ion track

formation in InP presented by Herre *et al.*³ Particularly, the TEM results shown there suggest that in the case of 250 MeV Xe irradiations at RT, continuous tracks extend up to depths of approximately 7 μm and discontinuous tracks reach a depth of about 10 μm . The electronic energy loss of the Xe ions at 7 and at 10 μm is 16.1 and 13.4 keV/nm, respectively (as calculated by the SRIM-2003 code). As suggested by Komarov *et al.*,¹² discontinuous tracks are formed due to statistical fluctuations of the SHI charge because of electron capture and loss processes. The statistical fluctuations of the ion charge are immediately followed by the corresponding fluctuations of the momentary energy loss ε_{mom} . Hence, if ε_{mom} is only slightly higher than the threshold value for track formation $\varepsilon_e^{\text{thr}}$, a capture of one or more electrons by a SHI can reduce ε_{mom} below $\varepsilon_e^{\text{thr}}$. Similarly, if ε_{mom} is only slightly lower than $\varepsilon_e^{\text{thr}}$, a loss of one or more electrons by a SHI can increase ε_{mom} so that it will be higher than $\varepsilon_e^{\text{thr}}$. In this way a discontinuous track is formed; the lengths of its isolated parts are determined by the probabilities of electron capture or loss⁴⁷ by a SHI. The mean energy loss at depth z is denoted as $\bar{\varepsilon}$ and its standard deviation as $\Delta\varepsilon$ ($\Delta\varepsilon > 0$). Then, discontinuous (continuous) tracks extend up to the depth where $(\bar{\varepsilon} \pm \Delta\varepsilon) = \varepsilon_e^{\text{thr}}$, respectively. Assuming that $\Delta\varepsilon(7 \mu\text{m}) = \Delta\varepsilon(10 \mu\text{m})$, the value of $\varepsilon_e^{\text{thr}}$ can be easily estimated for Xe irradiation: $\varepsilon_e^{\text{thr}} \cong (\bar{\varepsilon}(7 \mu\text{m}) + \bar{\varepsilon}(10 \mu\text{m}))/2 = (16.1 + 13.4 \text{ keV/nm})/2 \approx 14.8 \text{ keV/nm}$. This value corresponds to the energy loss of a Xe ion with an energy of ca. 100 MeV. Therefore, 100 MeV was taken to be the threshold energy for track formation in InP by Xe irradiation. Within the thermal spike model this means that the ion locally heats the target exactly up to the melting point T_m of 1335 K. This condition was used to determine τ_e . To do so, the value of τ_e is first set arbitrarily, and then changed in finite steps until the calculated maximum atomic temperature at the ion track axis equals T_m . The resulting value of τ_e ($8.5 \times 10^{-17} \text{ s}$) is used afterwards for all other ion species and energies; additionally, it is considered to be constant, because its temperature dependence is not known. Taking the calculated value of $6 \times 10^{22} \text{ cm}^{-3}$ as an estimation of the concentration of the freed electrons within ionization spikes (see Sec. IV), the electron-phonon coupling efficiency g can be calculated by using Eq. (17). Thus, for example, at the initial stage of the electron cooling the “hot” electrons can have temperatures up to 10^4 – 10^5 K , which leads to $g \approx (2.8 \times 10^{11})$ – $(2.8 \times 10^{12}) \text{ W/(cm}^3 \text{ K)}$. At the final stage of the electron cooling g amounts to ca. $9.3 \times 10^{13} \text{ W/(cm}^3 \text{ K)}$ when the electronic temperature approaches room temperature.

The initial and boundary conditions for both Eqs. (9) were chosen to be

$$T(r, 0) = T(R, t) = T_0, \quad \lim_{r \rightarrow 0} r^m K(T) \frac{\partial T}{\partial r} = 0, \quad (19)$$

where R is some constant value chosen arbitrarily so that $R \gg r_p$, and T_0 is the initial temperature of the target. The second condition in Eq. (19) demands that all spatial gradients of the temperature be finite.

The numerical solution of the system of differential equations (9) with the initial and boundary conditions (19) has

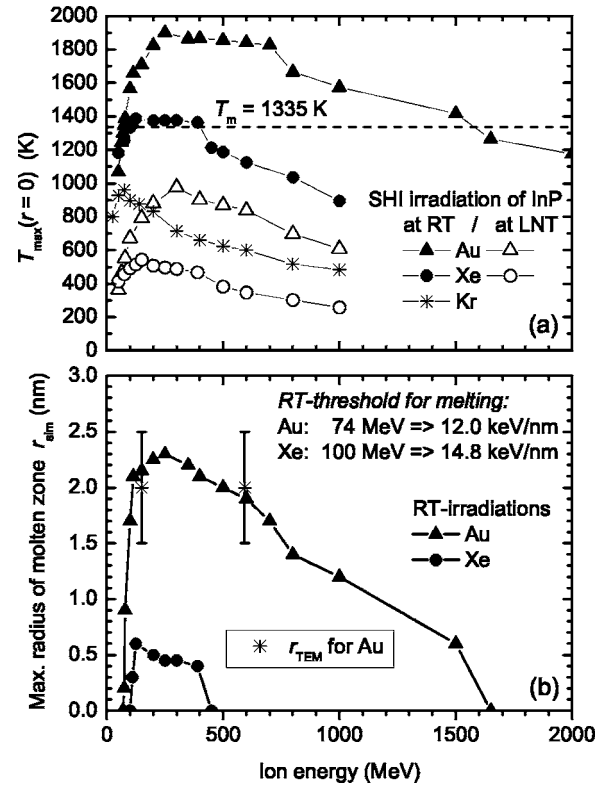


FIG. 12. (a) Dependence of the maximum atomic temperature at the ion track axis ($r=0$) on the ion energy for various ion species. The data are presented for both RT and LNT irradiations. The dashed line corresponds to the melting point of InP (1335 K). (b) Dependence of the maximum radius of the molten zone, r_{sim} , on the ion energy for various ion species. The data are shown solely for RT irradiations. The “low-energy” RT thresholds for melting are presented. Data points obtained from TEM for 150 and 593 MeV Au are also shown for comparison.

been performed using our program code HEAT.⁶⁷ We have used nonuniform spatial and uniform time grids. The constructed high accuracy scheme for the heat equations with variable coefficients was proven to be converging to the exact solution with the rate $O(h^2 + \tau)$, where h and τ are spatial and time grid steps, respectively. The details of the mathematical model can be found elsewhere.⁶⁷

VII. RESULTS OF THE CALCULATIONS

It has to be mentioned that in our calculations of the atomic temperature, the latent heat of melting is not taken into account. We have supposed that in order to melt material locally, it is enough to heat the atomic lattice up to the melting point. This can be qualitatively understood by keeping in mind that atoms located within an ionization spike have lost most of the valence electrons and, hence, the chemical bonding among ionized atoms must be much weaker than in the normal state.

The main results are depicted in Fig. 12. Part (a) of the figure shows the maximum atomic temperature at the ion track axis as a function of the ion species and energy. One can see that for RT irradiations with Au and Xe, the calcu-

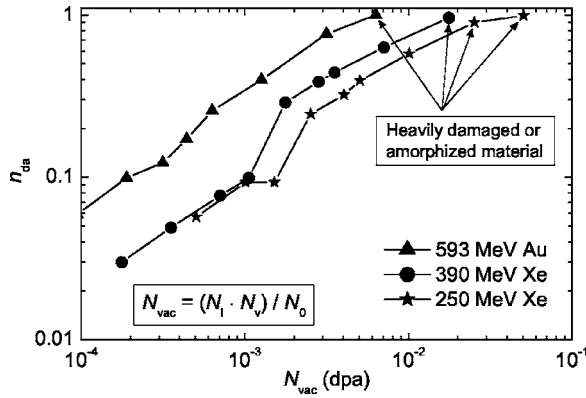


FIG. 13. Damage concentration (from RBS) vs calculated relative concentration of vacancies N_{vac} in units of displacements per atom (dpa).

lated maximum atomic temperatures exceed the melting point T_m within a certain range of ion energies. Conversely, for RT irradiations with Kr and for all LNT irradiations, the calculated maximum atomic temperatures are lower than T_m . Further, one can see that the maximum temperatures reached at the track axis differ by about 900 K for RT and LNT irradiations of InP with Au or Xe ions. This large difference is mainly due to the dependence of the thermal conductivity of the lattice on the temperature (at LNT, the thermal conductivity of the InP lattice is about seven times larger than at RT, as is shown in Fig. 11, i.e., at LNT the heat is transported away from the track core much more efficiently than at RT).

The resulting radii of the molten tracks formed by Au and Xe at RT are depicted in Fig. 12(b). It shows that the calculated radii vary with the ion species and energy.⁶⁸ Further, it demonstrates that there are “low-” and “high-energy” thresholds for melting, which are different for lighter and heavier ions. Finally, there appears to be no universal (i.e., valid for all ion species) “low-energy” RT threshold for melting (the only measure used commonly in the literature). More specifically, the threshold energy loss depends on the ion mass: $\varepsilon_e^{\text{thr}}$ is noticeably higher for lighter ions (cf. the estimated values of $\varepsilon_e^{\text{thr}}$ for Au and Xe of 12.0 and 14.8 keV/nm, respectively).

VIII. DISCUSSION

A. Origin of the radiation damage

As was shown in Sec. III A, SHI irradiation of virgin InP in an above-threshold electronic regime causes lattice disordering up to amorphization. In order to check for the possible influence of nuclear energy deposition, we recalculated the ion fluences N_l from Fig. 4(a) into relative concentrations of vacancies according to $N_{\text{vac}} = N_l N_v / N_0$, where N_v values were taken from Table I. Figure 13 shows the damage concentration n_{da} (resulting from RBS measurements) as a function of N_{vac} for some above-threshold irradiations. The data points $n_{\text{da}} \approx 1$ marked by arrows in the figure demonstrate that the material is already very heavily damaged or even amorphized, while the relative vacancy concentration is still very low: it amounts to only 0.5–3 % of the atomic density of InP.

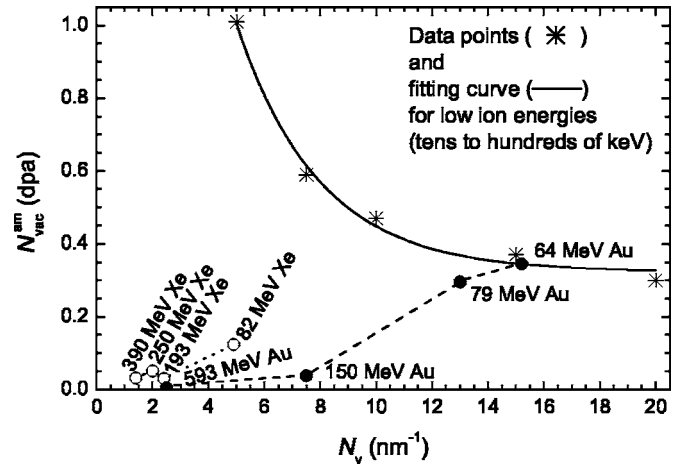


FIG. 14. Relative concentration of vacancies necessary for amorphization vs number of vacancies per ion and unit path length N_v (see Table I). The values of $N_{\text{vac}}^{\text{am}}$ were calculated according to $N_{\text{vac}}^{\text{am}} = N_l^{\text{am}} N_v / N_0$, where N_l^{am} is the ion fluence necessary for amorphization, and N_0 is the atomic density of InP. The data points for low ion energies are from Ref. 69.

The damage measured is too high to be caused by the nuclear energy loss of the ions. Therefore, the nuclear energy loss of the implanted ions cannot account for the damage formation illustrated in Fig. 13; instead, it has to be attributed to the high electronic energy deposition.⁹

Contrary to the above-threshold irradiations, in the case of subthreshold and near-threshold irradiations (i.e., for 82 MeV Xe, 64 MeV Au, and 79 MeV Au, see Table I) the nuclear energy loss of the ions can play a more important role, or can even turn into the dominating mechanism of damage formation. This is illustrated in Fig. 14, which shows the relative concentration of vacancies necessary for amorphization versus the number of vacancies per unit path length N_v . The results for low ion energies⁶⁹ of tens to hundreds of keV (where damaging is determined by nuclear energy loss) are shown for comparison. One can see in Fig. 14 that the data points for 64 and 79 MeV Au irradiations are very close to the curve for the low energies. Therefore, in those two cases the radiation damage is largely due to the nuclear energy loss, which qualitatively explains our observation that the experimental values $n_{\text{da}}(N_l)$ for 64/79 MeV Au irradiations cannot be fitted by single curves in the framework of the Gibbons’ model [see Sec. III A and Fig. 4(b)].

B. Formation and overlapping of ion tracks

Figure 15 shows a PV-TEM image of an InP sample irradiated with 593 MeV at RT. One can see in the figure both single ion tracks (marked by circles) and overlapping tracks (marked by arrows). The radii of the single isolated tracks were measured by a series of PV-TEM images taken with the same or higher magnification from various parts of the sample surface. The largest isolated tracks with radii of 3.0–4.5 nm are rather rare; their number does not exceed 5% of the total number of tracks. If the largest (very seldom observed) tracks⁴¹ are not taken into consideration, the radii

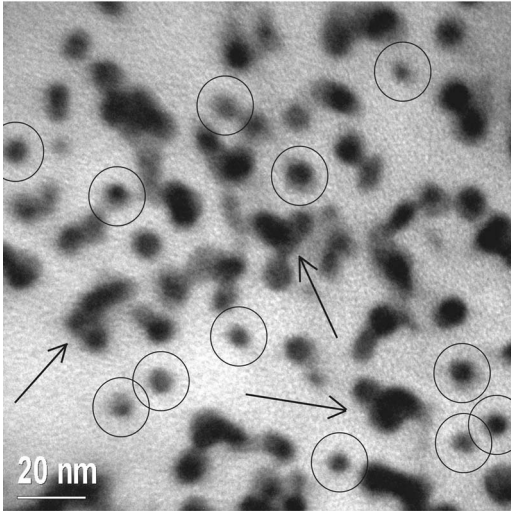


FIG. 15. PV-TEM image of an InP sample irradiated with 593 MeV Au at RT up to a fluence of $9 \times 10^{11} \text{ cm}^{-2}$. The circles mark single ion tracks and the arrows point to areas containing at least three to four overlapping tracks.

of smaller isolated tracks (that constitute the absolute majority of all isolated tracks) vary between 1.5 and 2.5 nm. The same range of isolated track radii is also observed for 150 MeV Au irradiations. Those values are in good agreement with the calculated radii of molten zones [see Fig. 12(b)].

Further, the calculated radii of molten zones in virgin InP irradiated with 193 MeV Xe, 250 MeV Xe, or 390 MeV Xe do not exceed 0.6 nm [see Fig. 12(b)]. This value is only slightly larger than the lattice constant of InP (0.587 nm). Therefore, not tracks, but rather point defects and point defect clusters are formed at first in virgin InP by fast Xe ions. This explains nicely the observed large discrepancy between the Xe ion fluence and the resulting number of registered ion tracks in InP (see Table III and Ref. 3). With increasing Xe ion fluence, more radiation damage is created in the form of point defects and point defect clusters, which increases the probability that subsequent Xe projectiles hit areas already damaged by preceding ions. Electrons freed by such ions from their host atoms no longer “see” the perfect virgin atomic lattice, but a more or less disordered one. Therefore, they interact more strongly with the atoms, causing a faster transfer of energy from excited electrons to the lattice, which favors the formation of visible tracks.

In terms of the thermal spike model, a more efficient transfer of energy from excited electrons to the lattice means that the electron-phonon coupling efficiency g [see Eq. (17)] becomes higher with increasing damage concentration. In order to estimate the qualitative influence of this effect on track formation, we have performed calculations with all the same parameters as previously (i.e., the results shown in Fig. 12), but multiplied the g values by a factor α_g . The values of molten track radii R_{sim} calculated in this way for selected ion species are shown in Fig. 16. The case of $\alpha_g = 1$ corresponds to SHI irradiations into perfectly ordered virgin material, while data points with $\alpha_g > 1$ are for predamaged InP. Finally, the data points for $\alpha_g < 1$ have no direct physical

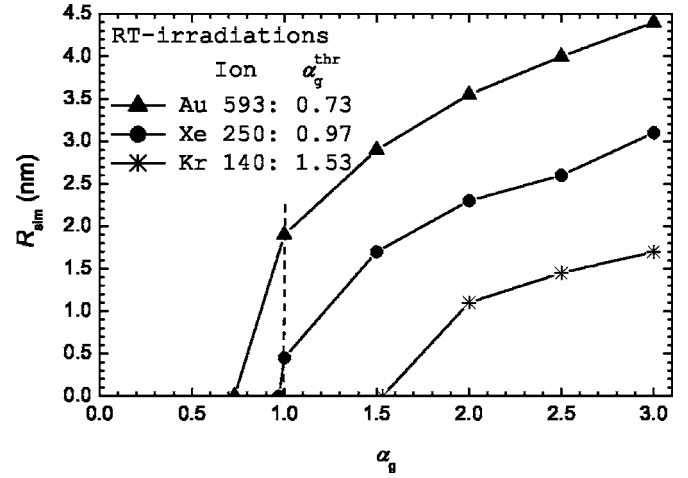


FIG. 16. Molten track radii calculated by the HEAT code in disordered InP assuming different predamage level and, hence, increased electron-phonon coupling efficiency g . The threshold values of the factor α_g are also shown (see text for details).

meaning, because the electron-phonon coupling efficiency cannot be lower than that for the perfectly ordered material. Nevertheless, the position at which the calculated curve crosses the abscissa, α_g^{thr} , allows us to predict whether a certain SHI irradiation of the virgin material will result in the track formation. One can expect rather continuous tracks if α_g^{thr} is noticeably lower than unity, rather discontinuous tracks if α_g^{thr} is close to unity, and, finally, no tracks are to be expected if this value is noticeably larger than unity. This conclusion is supported by the RBS and TEM investigations presented in this work and in Refs. 3–5. For example, no tracks in crystalline InP were formed by Kr irradiation with $\alpha_g^{\text{thr}} = 1.53$. However, even in this case tracks can be created if the ions penetrate heavily damaged areas or suffer an instantaneous loss of many electrons (though the latter event has a low probability).

The results obtained for LNT irradiations with 390 MeV Xe and 593 MeV Au show that the very first Xe or Au ions impinging perfectly ordered InP cannot create tracks, but only point defects and point defect clusters. This follows from the fact that, first, one overlap is necessary to fit the corresponding experimental $n_{\text{da}}(N_i)$ curves [see Fig. 4(b)] and, second, the calculations give radii of the molten zones of $r_{\text{sim}} = 0$ (see Fig. 12). This also explains why no tracks were observed by Gaiduk *et al.*⁵ in InP irradiated at LNT with a relatively low fluence of $7 \times 10^{12} \text{ cm}^{-2}$ of 250 MeV Xe ions. Conversely, subsequent Xe or Au ions are able to form discontinuous tracks at LNT (e.g., for the much higher Xe ion fluence of $3 \times 10^{13} \text{ cm}^{-2}$, see Figs. 7 and 8) by hitting damaged zones already created by preceding ions.

It is useful now to compare the values of the track radii obtained by the HEAT simulations with those resulting from RBS and TEM investigations. These values are summarized in Table IV. First, one can see that the simulated radii r_{sim} are generally lower than both r_{RBS} and r_{TEM} . However, the values of r_{sim} , r_{RBS} , and r_{TEM} for every certain ion species can in no way be equal to each other, because all of them have different physical meaning. So, the calculated radii r_{sim} are

TABLE IV. Ion track radii simulated by the HEAT code (r_{sim}), calculated from the respective RBS data (r_{RBS}), and measured by TEM (r_{TEM}) for different ion species. m_{RBS} is the number of overlaps obtained by fitting of the RBS data within the Gibbons' model for different SHI irradiations of InP.

Ion	E_1 (MeV)	T_I	m_{RBS}	r_{sim} (nm)	r_{RBS} (nm)	r_{TEM} (nm)
Xe	193	RT	0	0.50	1.2 ± 0.1	
Xe	250	RT	0	0.45	1.3 ± 0.1	2.2–4.0
Xe	390	RT	0	0.40	1.4 ± 0.1	
Au	150	RT	0	2.15	2.3 ± 0.1	1.5–3.5
Au	573	RT		1.92		1.5–4.5
Au	593	RT	0	1.90	3.0 ± 0.2	1.5–4.5
Xe	82	RT	1	0.0	1.6 ± 0.1	
Xe	390	LNT	1	0.0	0.9 ± 0.1	1.5–3.0
Au	593	LNT	1	0.0	3.9 ± 0.2	
Kr	140	RT		0.0		
Au	64	RT		0.0	1.2 ± 0.1	
Au	79	RT		0.9	1.1 ± 0.1	

exclusively for perfectly ordered material (see Fig. 12). Conversely, the data from the RBS investigations are more or less averaged values resulting from point defects, point defect clusters, and tracks (hence, the average track radius must be smaller than the respective value of r_{RBS}). Finally, the TEM data cover the range from the narrowest tracks (formed by single ions hitting undamaged crystalline areas) to wider ones (due to multiple ions hitting the same area). The diameters of the tracks vary over a broad range. Furthermore, for discontinuous tracks the general picture is even more complex, because their second spatial dimension (length) is also varied. Nevertheless, as expected, in those cases where each ion is supposed to produce a track (noticeably larger than point defect clusters and large enough to be stable, as seems to be the case, e.g., for RT irradiations with 150 MeV and 593 MeV Au), the calculated radii r_{sim} are close to the lower limit of the TEM radii r_{TEM} . Conversely, for SHI irradiations with ion species producing at first no amorphous tracks but rather point defect clusters in *perfectly ordered virgin* material (all RT and LNT irradiations with Xe, and LNT irradiations with 593 MeV Au), the values of r_{sim} and r_{RBS} are generally smaller than the radii deduced from TEM studies.

IX. CONCLUSIONS

It is shown that the experimental data obtained for InP can be qualitatively and quantitatively described on the basis of the inelastic thermal spike (TS) model that has been originally used only for metallic targets. The presented extension of the TS model on semiconductors covers mainly the very first stage of the energy transfer from SHI's (so-called "ionization spikes").

We show that the extended TS model successfully describes the track formation and the damage accumulation in the III-V binary semiconductor InP. The most important input parameters necessary for the modeling are deduced from available experimental data. The calculated values of the ion

track radii are in good agreement with the presented RBS and TEM results, and with the experimental results published by other authors. Our results show that the extended TS model offers a self-consistent way to explain the influence of various irradiation conditions (ion mass, ion energy, irradiation temperature, etc.) on the ion track formation and damage accumulation in InP and, therefore, can make a contribution to a better understanding of the underlying mechanisms.

Further, our results prejudice the amenity of a *single value* of the threshold LET $\varepsilon_e^{\text{thr}}$ as a fundamental quantity that is commonly used for the description of track formation in solids irradiated with *different ion species*. So, it is shown that there is no universal RT threshold for track formation in InP. More specifically, the threshold energy loss depends on the ion mass: $\varepsilon_e^{\text{thr}}$ is noticeably higher for lighter ions (12.0 and 14.8 keV/nm for RT irradiations with Au and Xe, respectively).

The experimental data and the results of the simulation of the radii of ion tracks formed by Xe irradiation in virgin InP nicely explain the observed large discrepancy between the Xe ion fluence and the resulting number of registered ion tracks in InP. Finally, our experimental and simulation results on the LNT irradiations as well as on the subthreshold irradiations at RT support the idea that the formation of visible tracks requires a predamaging⁴ of the material, unless each SHI penetrating *perfectly ordered virgin* InP directly produces a track that is noticeably larger than point defect clusters and large enough to be stable.

ACKNOWLEDGMENTS

The authors thank S. Klaumünzer and A. Hedler for the experimental support during the SHI irradiations, and O.V. Milchanin for a part of the TEM investigations. This work was supported by the Bundesministerium für Bildung und Forschung (Contract No. 05KK1SJA/2) and by the Deutsche Forschungsgemeinschaft (Contract No. WE 1707/8-1).

- ¹Though “electronic energy deposition” has a broader meaning, in the present paper this term will be used exclusively as a synonym of linear energy transfer (LET, in units of energy/length) and is denoted as ε_e .
- ²D. Streit, *Compound Semicond.*, May (2002); D. Lammers, *Electronic Engineering Times*, September (2002); B. Humphreys and A. O’Donell, *Compound Semicond.*, August (2003); T. Whittaker, *Compound Semicond.*, January (2004); D. Lammers, *Electronic Engineering Times*, March (2004).
- ³O. Herre, W. Wesch, E. Wendler, P. I. Gaiduk, F. F. Komarov, S. Klaumünzer, and P. Meier, *Phys. Rev. B* **58**, 4832 (1998).
- ⁴W. Wesch, O. Herre, P. I. Gaiduk, E. Wendler, S. Klaumünzer, and P. Meier, *Nucl. Instrum. Methods Phys. Res. B* **146**, 341 (1998).
- ⁵P. I. Gaiduk, F. F. Komarov, and W. Wesch, *Nucl. Instrum. Methods Phys. Res. B* **164-165**, 377 (2000).
- ⁶G. Szenes, Z. E. Horváth, B. Pécz, F. Pászti, and L. Tóth, *Phys. Rev. B* **65**, 045206 (2002).
- ⁷W. Wesch, A. Kamarou, E. Wendler, K. Gärtner, P. I. Gaiduk, and S. Klaumünzer, *Nucl. Instrum. Methods Phys. Res. B* **206**, 1018 (2003).
- ⁸W. Wesch, A. Kamarou, and E. Wendler, *Nucl. Instrum. Methods Phys. Res. B* **225**, 111 (2004).
- ⁹A. Kamarou, W. Wesch, E. Wendler, and S. Klaumünzer, *Nucl. Instrum. Methods Phys. Res. B* **225**, 129 (2004).
- ¹⁰A. S. Khalil, D. J. Llewellyn, M. C. Ridgway, A. M. Stewart, A. P. Byrne, and L. T. Chadderton, *Microsc. Microanal.* **10**, Suppl. S02, 580 (2004).
- ¹¹A. Kamarou, E. Wendler, and W. Wesch, *J. Appl. Phys.* **97**, 123532 (2005).
- ¹²F. F. Komarov and A. F. Komarov, *J. Exp. Theor. Phys.* **86**, 270 (1998).
- ¹³F. F. Komarov, A. F. Komarov, and A. M. Mironov, *Nucl. Instrum. Methods Phys. Res. B* **148**, 159 (1999).
- ¹⁴A. Meftah, F. Brisard, J. M. Costantini, M. Hage-Ali, J. P. Stoquert, F. Studer, and M. Toulemonde, *Phys. Rev. B* **48**, 920 (1993).
- ¹⁵R. L. Fleischer, P. B. Price, and R. M. Walker, *Nuclear Tracks in Solids* (University of California Press, Berkeley, CA, 1975).
- ¹⁶R. E. Johnson and W. L. Brown, *Nucl. Instrum. Methods Phys. Res.* **198**, 103 (1982).
- ¹⁷D. Lesueur and A. Dunlop, *Radiat. Eff. Defects Solids* **126**, 163 (1993).
- ¹⁸Y. Kitazoe, N. Hiraoka, and Y. Yamamura, *Surf. Sci.* **111**, 381 (1981).
- ¹⁹Y. Yamamura, *Nucl. Instrum. Methods Phys. Res.* **194**, 515 (1982).
- ²⁰I. S. Bitensky and E. S. Parilis, *Nucl. Instrum. Methods Phys. Res. B* **21**, 26 (1987).
- ²¹C. C. Watson and T. A. Tombrello, *Radiat. Eff.* **89**, 263 (1985).
- ²²P. Stampfli and K. H. Bennemann, *Phys. Rev. B* **49**, 7299 (1994).
- ²³P. Stampfli, *Nucl. Instrum. Methods Phys. Res. B* **107**, 138 (1996).
- ²⁴M. Toulemonde, C. Dufour, and E. Paumier, *Phys. Rev. B* **46**, 14362 (1992).
- ²⁵Ch. Dufour, E. Paumier, and M. Toulemonde, *Nucl. Instrum. Methods Phys. Res. B* **122**, 445 (1997).
- ²⁶C. Dufour, A. Audouard, F. Beuneu, J. Dural, J. P. Girard, A. Hairie, M. Levalois, E. Paumier, and M. Toulemonde, *J. Phys.: Condens. Matter* **5**, 4573 (1993).
- ²⁷A. Meftah, F. Brisard, J. M. Costantini, E. Dooryhee, M. Hage-Ali, M. Hervieu, J. P. Stoquert, F. Studer, and M. Toulemonde, *Phys. Rev. B* **49**, 12457 (1994).
- ²⁸Z. G. Wang, Ch. Dufour, E. Paumier, and M. Toulemonde, *J. Phys.: Condens. Matter* **6**, 6733 (1994).
- ²⁹M. Toulemonde, Ch. Dufour, Z. Wang, and E. Paumier, *Nucl. Instrum. Methods Phys. Res. B* **112**, 26 (1996).
- ³⁰A. Meftah, J. M. Costantini, M. Djebara, N. Khalfaoui, J. P. Stoquert, F. Studer, and M. Toulemonde, *Nucl. Instrum. Methods Phys. Res. B* **122**, 470 (1997).
- ³¹E. M. Bringa and R. E. Johnson, *Nucl. Instrum. Methods Phys. Res. B* **143**, 513 (1998).
- ³²E. M. Bringa and R. E. Johnson, *Phys. Rev. Lett.* **88**, 165501 (2002).
- ³³A. Miotello, R. Kelly, and M. Dapor, *Nucl. Instrum. Methods Phys. Res. B* **141**, 16 (1998).
- ³⁴J. P. Biersack and J. F. Ziegler, *The Stopping and Ranges of Ions in Matter* (Pergamon Press, Oxford, 1985), Vol. 1.
- ³⁵B. Massarani and J. C. Bourgoin, *Phys. Rev. B* **34**, 2470 (1986).
- ³⁶K. Gärtner, *Nucl. Instrum. Methods Phys. Res. B* **132**, 147 (1997).
- ³⁷G. Schiwietz, K. Czerski, M. Roth, F. Staufenbiel, and P. L. Grande, *Nucl. Instrum. Methods Phys. Res. B* **226**, 683 (2004).
- ³⁸J. F. Gibbons, *Proc. IEEE* **60**, 1062 (1972).
- ³⁹I. Jenčič, E. P. Hollar, and I. M. Robertson, *Philos. Mag.* **83**, 2557 (2003).
- ⁴⁰Because of overlapping tracks, we were able to estimate only the lower limit in their surface density. Nevertheless, in the case of the irradiation with 573 MeV Au ions in the equilibrium charge state and with relatively low ion fluence of $1 \times 10^{11} \text{ cm}^{-2}$ (see Tables I and III), the ion tracks almost do not overlap and, therefore, can be counted more accurately. In this case the number of ion tracks is $\geq 9 \times 10^{10} \text{ cm}^{-2}$ (see Fig. 7). Taking into account the experimental error for the estimation of the ion fluence ($\pm 10\%$), one can conclude that each 573-MeV Au ion produces a visible track.
- ⁴¹The ion track radii determined from PV-TEM images are exclusively for isolated tracks. However, one cannot exclude the possibility that the largest isolated tracks are due to multiple projectiles hitting the sample surface at the same point or very close to it. One further probable explanation of the variation in the isolated track radii is the inevitable phenomenon of ion charge fluctuations that increase or decrease the momentary energy loss and in this way statistically alter the track radii.
- ⁴²G. Schiwietz, E. Luderer, G. Xiao, and P. L. Grande, *Nucl. Instrum. Methods Phys. Res. B* **175-177**, 1 (2001).
- ⁴³M. Raff, M. Schütze, C. Trappe, R. Hannot, and H. Kurz, *Phys. Rev. B* **50**, 11031 (1994).
- ⁴⁴K. Sokolowski-Tinten, J. Bialkowski, and D. von der Linde, *Phys. Rev. B* **51**, 14186 (1995).
- ⁴⁵L. Huang, J. P. Callan, E. N. Glezer, and E. Mazur, *Phys. Rev. Lett.* **80**, 185 (1998).
- ⁴⁶M. P. R. Waligorski, R. N. Hamm, and R. Katz, *Nucl. Tracks Radiat. Meas.* **11**, 309 (1986).
- ⁴⁷H. D. Betz, *Rev. Mod. Phys.* **44**, 465 (1972).
- ⁴⁸S. P. Ahlen, *Rev. Mod. Phys.* **52**, 121 (1980).
- ⁴⁹P. Sigmund, A. Fettouhi, and A. Schinner, *Nucl. Instrum. Methods Phys. Res. B* **209**, 19 (2003).
- ⁵⁰D. Drouin, A. R. Couture, R. Gauvin, P. Hovington, P. Horny, and H. Demers, computer code CASINO, version 2.42 (2002); <http://www.gel.usherbrooke.ca/casino/index.html>.

- ⁵¹P. L. Grande and G. Schiwietz, Nucl. Instrum. Methods Phys. Res. B **195**, 55 (2002).
- ⁵²The electron shell binding energies $I^{(i)}$ for elements were taken from G. Williams' WWW compilation (see <http://www.jlab.org/~gwyn/ebindene.html> or <http://www.webelements.com>).
- ⁵³K. Gärtner, in *Physical Research Series*, Vol. 6: *High Energy Ion Beam Analysis of Solids*, edited by G. Götz and K. Gärtner (Akademie-Verlag, Berlin, 1988), p. 29.
- ⁵⁴M. G. Holland, Phys. Rev. **134**, A471 (1964).
- ⁵⁵A. Amith, I. Kudman, and E. F. Steigmeier, Phys. Rev. **138**, A1270 (1965).
- ⁵⁶T. Elsaesser and M. Woerner, Phys. Rep. **321**, 253 (1999).
- ⁵⁷A. Chatterjee and H. J. Schaefer, Radiat. Environ. Biophys. **13**, 215 (1976).
- ⁵⁸F. Studer, M. Hervieu, J.-M. Costantini, and M. Toulemonde, Nucl. Instrum. Methods Phys. Res. B **122**, 449 (1997).
- ⁵⁹C. Trautmann, M. Toulemonde, K. Schwartz, J. M. Costantini, and A. Müller, Nucl. Instrum. Methods Phys. Res. B **164**, 365 (2000).
- ⁶⁰M. I. Kaganov, I. M. Lifshitz, and L. V. Tanatarov, Sov. Phys. JETP **4**, 173 (1957).
- ⁶¹I. A. Baranov, Yu. V. Martinenko, S. O. Tsepelevitch, and Yu. N. Yavlinskii, Sov. Phys. Usp. **31**, 1015 (1988).
- ⁶²*Landolt-Börnstein: Numerical Data and Functional Relationships in Science and Technology—New Series*, Group III: Condensed Matter (Springer-Verlag, Berlin, 1984), Vol. 17d.
- ⁶³S. Adao, *Physical Properties of III-V Semiconductor Compounds: InP, InAs, GaAs, GaP, InGaAs, and InGaAsP* (John Wiley & Sons, New York, 1992), pp. 49-56.
- ⁶⁴S. E. Laux and M. V. Fischetti, computer code DAMOCLES (see Table 7 in “Numerical part” at http://www.research.ibm.com/DAMOCLES/html_files/numerics.html#table7)
- ⁶⁵K. Izui, J. Phys. Soc. Jpn. **20**, 915 (1965).
- ⁶⁶Because of the applied uniform time grid to be mentioned below, taking 5×10^{-15} s instead of 1×10^{-15} s allows us to use five times larger time steps in the finite difference schemes for Eqs. (9) and, hence, results in a very substantial saving of the processor time.
- ⁶⁷A. A. Kamarou, D. A. Malafei, and V. S. Shcheklik, in *Proceedings of the 2nd International Conference on Finite-Difference Methods: Theory and Applications, 1998* (Minsk, Belarus), Vol. 2, pp. 56–62.
- ⁶⁸Similar calculations were performed for Pb irradiations at RT as well. The corresponding line for Pb lies only slightly above that for Au and, therefore, it is omitted in the figure. For example, the calculated track radii amount to 2.4 nm (not shown) in the case of 385 MeV Pb irradiation at RT and, hence, are in good agreement with the TEM results presented by Szenes *et al.*, (see Ref. 6).
- ⁶⁹E. Wendler, T. Opfermann, and P. I. Gaiduk, J. Appl. Phys. **82**, 5965 (1997).